Journal of Vibration Testing and System Dynamics

Journal homepage: https://lhscientificpublishing.com/Journals/JVTSD-Default.aspx

Feasibility of controlling gas concentration and temperature distributions in a semiconductor chamber with CT-TDLAS

Daisuke Hayashi[1, 2†], Junya Nakai[1], Masakazu Minami[1], Takahiro Kamimoto[2], Yoshihiro Deguchi[2]

[1] HORIBA STEC, Co., Ltd., Kyoto 601-8116, Japan

[2]Graduate School of Advanced Technology and Science, Tokushima University, Tokushima, 770-8506, Japan

Submission Info

Communicated by
Received
Accepted

Available online

Keywords

Laser spectroscopy
Semiconductor process
Computed Tomography

Abstract

The feasibility to control the gas concentration and temperature distributions in a semiconductor process chamber by measuring them was investigated. Gas concentration and temperature distributions for various flow rates were measured with the computed tomography-tunable diode laser absorption spectroscopy (CT-TDLAS). The infrared absorption spectra of multiple laser paths passing through the measured area were collected and the distributions of methane concentration and temperature in the chamber were reconstructed with the computed tomography (CT) calculations. The measured results indicated that the distributions can be independently controlled by measuring with the CT-TDLAS and adjusting the flow rates and the susceptor temperature.

1. Introduction

With increasing integration densities of semiconductor devices, the fabrication processes have become more and more complicated. For example, the dry etching [1-5] plays important roles in fabricating the fine structures of integrated devices like three-dimensional NOT-AND flash memories or fin-type field effect transistors. On this process, several kinds of reactive molecules, ions, and electrons radically collide with each other in gas and plasma phase. To achieve the target structures, the precise tuning of process parameters including gas flow rates, pressure, temperature, and radiative frequency power is critical. However, determining the optimal parameters for such complex process is quite difficult, and the condition in the chamber can drift during the process or run-to-run repetitions [6, 7]. The virtual metrology using large scale statistical data processing [8-11] have been utilized as a method to determine the parameters. However, the best way is to measure conditions inside the chamber and adjust process parameters in-situ. In-situ measurements for concentration of gas species [12-14] or plasma radicals [15, 16] in etching chambers using mid-infrared laser spectroscopy have been reported.

Semiconductor wafer yield is directly affected by spatial gas distributions [17, 18]. The distributions can be measured in-situ with computed tomography-tunable diode laser absorption spectroscopy (CT-TDLAS) [19]. In this method, the infrared absorption spectra for multiple laser paths passing through the measured area are collected. The spatial distributions of gas concentration and temperature are reconstructed with computed to-

† Corresponding author.
Email address: daisuke.hayashi@horiba.com

mography (CT) calculations from the collected spectra. This method has been adopted for analyses of combustion fields [22-27], vehicle engine exhausts [29-32], and diagnosis of an aero-propulsion engine [33]. In previous works, the CT-TDLAS was applied to measure methane (CH_4) concentration and temperature distributions in a semiconductor chamber [34, 35]. The measured results clearly showed that the distributions were varied according to the locations of CH_4 feeding ports and heater blocks on the susceptor. However, the experiments were made under the fixed gas flow rates. If the distributions can be varied by changing the gas flow rates, the control of the distributions by adjusting the gas flow rates is possible.

In this work, the feasibility to control the concentration and temperature distributions in the semiconductor chamber by measuring them with the CT-TDLAS was investigated. CH_4 concentration and temperature distributions were measured inside the chamber for various flow rates, and the possibility to control the distributions was discussed. To focus on the feasibility study, the gas species and the pressure inside the chamber were limited in the experiments. The paper is organized as follows. In section 2, the theoretical background of the CT-TDLAS is described. In section 3, the experimental setup including the chamber structure and gas flow system is explained. In section 4, the distributions for various flow rates under fixed conditions of CH_4 concentrations injected from the inlet ports and the susceptor temperature were simulated with the computer fluid dynamics (CFD). The CT algorithm was applied to the simulated distributions to examine the reproducibility and limitation of the CT. In section 5, CH_4 was actually streamed to measure the concentration and temperature distributions in the chamber under the same conditions. Based on the results, the feasibility to control the concentration and temperature distributions in the semiconductor chamber was discussed.

2. Theoretical backgrounds

2.1 Basics

The absorbance of light, A, passing through a gas at a wavelength λ is related to the gas concentration C as [36]

$$A(\lambda) = \log\left(\frac{I_0(\lambda)}{I(\lambda)}\right) \tag{1}$$

$$= CLP\sum_{j\in\lambda} S_j(T)G_{vj}, \tag{2}$$

where I_0 and I are incident and transmitted light intensity, L is the path length, P is the pressure, $S_j(T)$ is the absorption line strength of transition j at temperature T, and G_{vj} is the line broadening function. The absorbance is proportional to the concentration, and the absorption line strength of each transition has different temperature dependence. Therefore, by measuring the spectrum including more than two absorption wavelengths, concentration and temperature of the gas are simultaneously determined [37-41].

In the CT-TDLAS, multiple laser paths are intersected with each other in the measured area. The integrated absorbance for each path $A_p^{(meas)}(\lambda)$ (p is the path index) is measured by scanning the laser wavelength. On the other hand, when the concentration and temperature distributions are given, the integrated absorbance can be calculated: the distributions of concentration $C(x,y)$ and temperature $T(x,y)$ at a grid (x,y) are approximated in the form of polynomials as

$$C(x,y) = \sum_{l>m} a_{lm}x^{l-m}y^m, \tag{3}$$

$$T(x,y) = \sum_{l>m} b_{lm}x^{l-m}y^m. \tag{4}$$

Here l,m are the polynomial order. Twelfth-order polynomials were employed in this study. The integrated absorbance $A_p^{(cal)}(\lambda)$ over path p is calculated from

$$A_p^{(cal)}(\lambda) = \int_{(x,y)\in p} C(x,y)\alpha\big(\lambda, P, T(x,y)\big)dl, \tag{5}$$

where $\alpha(\lambda, P, T)$ is the absorbance per unit concentration per unit length that is referred from the database prepared in advance. The details of the database are described in Ref. [35]. The distributions of $C(x,y)$ and $T(x,y)$ are determined so that the square error defined as

$$E = \sum_p \int \left\{A_p^{(meas)}(\lambda) - A_p^{(cal)}(\lambda)\right\}^2 d\,\lambda, \tag{6}$$

is minimized.

2.2 Measures for rapid calculation

Rapid processing of the CT calculation is essential to control the distributions in the chamber from the measured results. The following describes the practical measures for rapid calculation.

2.2.1 Gradient method

In the CT calculation, arbitrary concentration and temperature distributions having the coefficient sets of $\{a_{lm}\}$ and $\{b_{lm}\}$ are given as initial ones, then updated iteratively until the square error is minimized. To achieve the minimum square error as rapidly as possible, the distributions are updated so that the square error is decreased in the manner of the gradient method, i.e., they are changed to follow the steepest descent direction in the E with respect to $\{a_{lm}\}$ and $\{b_{lm}\}$,

$$a_{lm} := a_{lm} - \eta \frac{\partial E}{\partial a_{lm}}, \tag{7}$$

$$b_{lm} := b_{lm} - \eta \frac{\partial E}{\partial b_{lm}}, \tag{8}$$

where η is the constant called the learning rate. In this study, $\eta = 1.0 \times 10^{-4}$ was adopted. The outline of the procedure is summarized in Fig. 1.

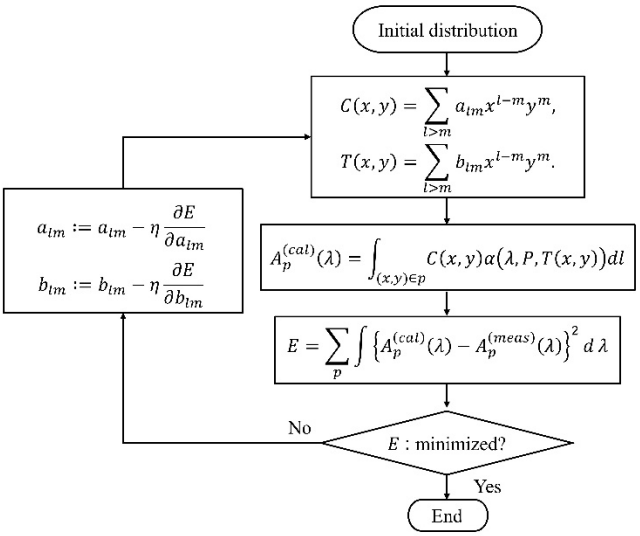

Fig. 1. Flow chart of CT calculation.

2.2.2 Determination of initial distributions

The initial distributions are determined using the path averaged concentrations and temperatures calculated from the measured spectra. First, they were set as linear combinations [32]

$$C^{(ini)}(x, y, \vec{u}) = \sum_k u_k C^{(k)}(x, y), \tag{9}$$

$$T^{(ini)}(x, y, \vec{v}) = \sum_k v_k T^{(k)}(x, y), \tag{10}$$

where $C^{(k)}(x, y)$, $T^{(k)}(x, y)$ are arbitrary distribution patterns (k is the index of the pattern), and $\vec{u} = (u_0, u_1, \cdots), \vec{v} = (v_0, v_1, \cdots)$ are the weight coefficient vectors. Next, $\vec{u}$ and $\vec{v}$ were determined to minimize the differences between the path averages $\bar{C}_p^{(ini)}$, $\bar{T}_p^{(ini)}$ and the measured path averages $\bar{C}_p^{(meas)}$, $\bar{T}_p^{(meas)}$, which were calculated from the relation

$$A_p^{(meas)}(\lambda) = \bar{C}_p^{(meas)} \alpha \left(\lambda, P, \bar{T}_p^{(meas)}\right) L_p. \tag{11}$$

Here L_p is the length of path p.

3. Experimental setup

The schematic of the CT-TDLAS measurement system is shown in Fig. 2. Distributed feedback laser diodes (DFB-LDs) at 1628 nm and 1654 nm (NTT Electronics Co., NLK1U5EAAA) were employed as the laser sources. Their wavelengths were scanned by driving current modulation around the CH_4 absorption wavelengths of 1628.1 nm and 1653.7 nm. Continuous saw tooth waveforms with a frequency of 0.5 kHz were used for the modulation. The two modulation signals were synchronized but their directions of the current variation were opposite with each other. The two laser beams were combined by a fiber combiner, and separated into 32 paths by a fiber splitter, then injected into the 32-laser-path cell through collimators. The collimators were placed in four different directions of the cell at 45° intervals. The injected laser beams passed through the measured area, and were detected by 32 photodiodes (PDs, Hamamatsu, G12180-010SPL). The detected signals were stored by a recording system (National Instruments, cRIO-9035) with sampling rate of 500 kHz. The structures of the chamber are shown in Figs. 3 (a), (b). The chamber has five ports on the top of the upper lid. The center port was for attaching a pressure gauge, and the other four were gas inlet ports that were located with cyclic symmetry on a circle of 60 mm-diameter. Figure 3 (b) shows the 32-laser-path cell installed in the chamber together with the susceptor which was placed at the bottom of the measured area. The cell was sandwiched by upper and lower panels of the chamber via O-rings. The measured area was inside the center circle whose diameter was 100 mm. The area was surrounded by a silica crystal ring. Thirty-two collimators and PDs were attached around the cell and the 32 laser-paths were intersected in the measured area. The vertical distance between the laser path and the upper surface of the susceptor was about 1 mm or less. The main body of the susceptor was made of poly-ether-ether-ketone (PEEK) for heat insulation. Four aluminum heater blocks were embedded in the susceptor, and their temperatures were independently regulated. Four gas exhaust holes were also laid between the heater blocks and just under the four inlet ports. The centers of the heater blocks and the exhaust ports were configured on the same circle of 60 mm-diameter.

The gas flow system is illustrated in Fig 4. CH_4 diluted by nitrogen (N_2) was introduced into the chamber, and the flow rate was controlled by mass flow controllers placed in the upstream of the chamber. The pressure in the chamber was regulated at 101.3 kPa by a back pressure regulator. The cables for thermocouples and heaters for regulating the heater blocks passed through an exhaust pipe below the chamber, and were extracted through cable extraction ports in order to seal off the inside the pipe.

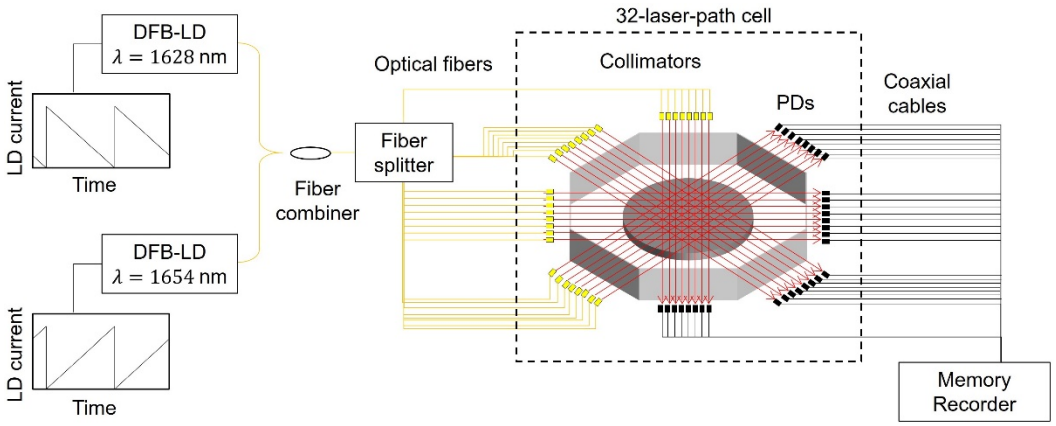

Fig. 2 Schematic of CT-TDLAS measurement system.

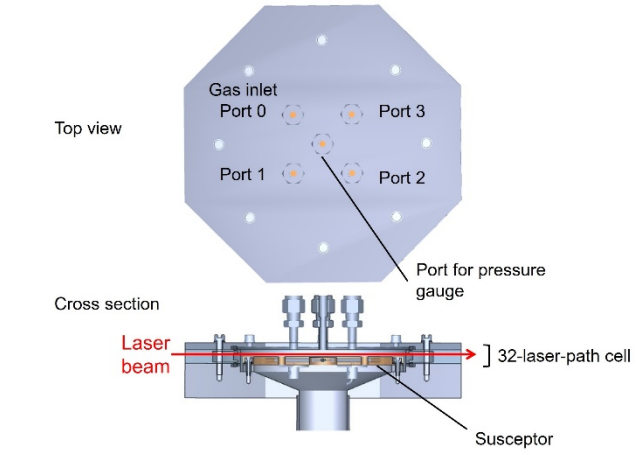

(a)

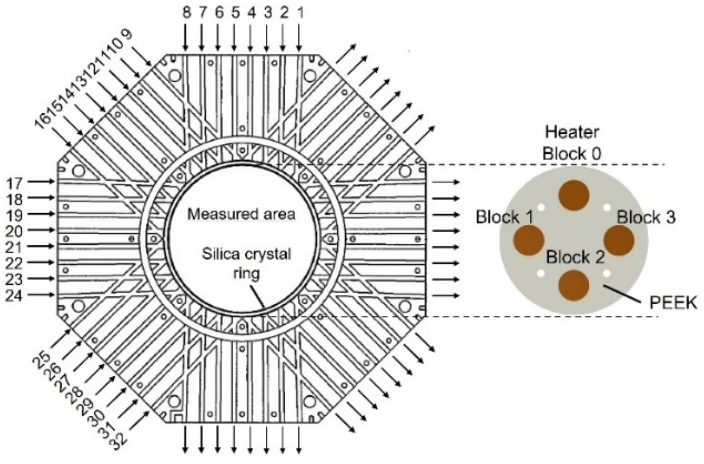

(b)

Fig. 3 (a) Structure of the chamber. **(b)** 32-laser-path cell. Numbers and arrows indicate path number and laser beam directions, respectively (left). The susceptor. Four small spots between heater blocks are exhaust holes (right).

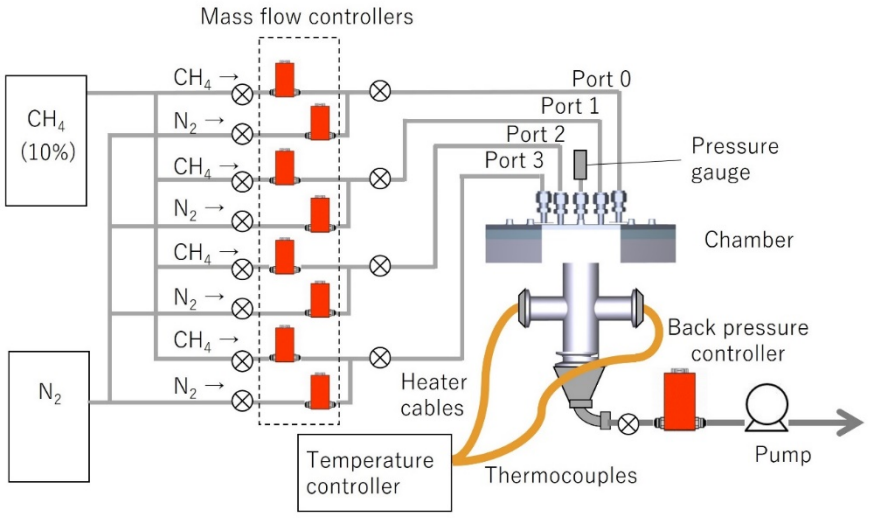

Fig. 4 Gas flow system of the chamber.

4. Reproducibility and limitation of the CT reconstruction

CH_4 concentration and temperature distributions for various flow rates were simulated with the CFD (FloFED, Mentor Graphics). The conditions of CH_4 flow rates are listed in Table 1, and CH_4 concentrations injected from the ports, the temperatures of heater blocks were shown as Fig. 5. The governing equations of the CFD are as follows:

$$\frac{\partial \rho}{\partial t} + \frac{\partial (\rho u_{i_1})}{\partial x_{i_1}} = 0, \tag{12}$$

$$\frac{\partial (\rho u_{i_1})}{\partial t} + \frac{\partial (u_{i_2} \rho u_{i_1})}{\partial x_{i_1}} = -\frac{\partial p}{\partial x_{i_1}} + \frac{\partial}{\partial x_{i_1}} \left(\mu \frac{\partial u_{i_1}}{\partial x_{i_2}} \right) - \rho g_{i_1} \beta (T - T_0), \tag{13}$$

$$\frac{\partial (\rho C_p T)}{\partial t} + \frac{\partial (\rho u_{i_1} C_p T)}{\partial x_{i_1}} = \frac{\partial}{\partial x_{i_1}} \left(\kappa \frac{\partial T}{\partial x_{i_1}} \right) + H. \tag{14}$$

These equations determine the behavior of ρ (density), u (velocity), p, and T of CH_4. Here, μ is the viscosity coefficient, g is the gravity, β is the thermal expansion coefficient, T_0 is the initial temperature, C_p is the heat capacity, κ is the heat conductivity, H is the enthalpy. Indices $i_1, i_2 = 1, 2, 3$ correspond to x, y, z components. This simulation was made under the assumption that the inner wall was no-slip and the thermal radiation effect was negligible [35]. The results are shown in Fig. 6. In all simulated distributions, high concentrations around the port 0 and high temperatures around the block 0 were obtained. When comparing the concentrations of condition 1, 2, and 3, the high concentration area became larger in the order of 1→2→3. On the other hand, when comparing the concentrations of condition 1, 4, and 5, the area became smaller in the order of 1→4→5. The reasons of these behaviors are that small (large) flow rates of ports 1-3 enhanced (disturbed) the spread of high concentration CH_4 injected from port 0. The temperature distributions were almost the same throughout all conditions, and independent of the concentration distribution variations.

Next, the spectra of the 32 paths for the simulated distributions were calculated using Eq. (5). Based on the spectra, the concentration and temperature distributions were reconstructed with the CT calculation. The reconstructed distributions are shown in Fig. 7. The CT reconstructed the overall characteristics of the CFD distributions. However, the reconstruction of concentration distributions in condition 4 and 5 looks poor especially

around the port 0. To quantitatively evaluate the similarities between the simulated and reconstructed distributions, the sum of squared difference (SSD) and the zero-mean normalized cross-correlation (ZNCC) were calculated for each condition [28]. The SSD is defined as

$$SSD = \frac{1}{X_{max}} \sqrt{\frac{1}{N_1 N_2} \sum_{n_1=0}^{N_1-1} \sum_{n_2=0}^{N_2-1} \left\{ \left(X_{n_1 n_2}\right)_{CFD} - \left(X_{n_1 n_2}\right)_{CT} \right\}^2}. \quad (15)$$

Here $X_{n_1 n_2}$ is the concentration or temperature at each grid, X_{max} is the maximum values in the CFD distribution, N_1 and N_2 are the total numbers of meshes along the x- and y-axis set in the measured area, respectively. If the SSD is close to "0", the two patterns can be considered as almost the same. The ZNCC is defined as

$$ZNCC = \frac{\sum_{n_1=0}^{N_1-1} \sum_{n_2=0}^{N_2-1} \left\{ \left(X_{n_1 n_2} - \overline{X}\right)_{CFD} \left(X_{n_1 n_2} - \overline{X}\right)_{CT} \right\}}{\sqrt{\sum_{n_1=0}^{N_1-1} \sum_{n_2=0}^{N_2-1} \left(X_{n_1 n_2} - \overline{X}\right)_{CFD}^2 \sum_{n_1=0}^{N_1-1} \sum_{n_2=0}^{N_2-1} \left(X_{n_1 n_2} - \overline{X}\right)_{CT}^2}}, \quad (16)$$

where

$$\overline{X} = \frac{1}{N_1 N_2} \sum_{n_1=0}^{N_1-1} \sum_{n_2=0}^{N_2-1} X_{n_1 n_2}. \quad (17)$$

If the ZNCC is close to "1", the correlation between the two is high, and they can be considered as almost the same. In this evaluation, the measured area were discretized by 2.5 mm mesh along the x- and y-axis. The total number of meshed grid ($= N_1 N_2$) was 1257. The calculated SSDs and ZNCCs are shown in Table 2. As good SSDs of lower than 0.05 were obtained for all distributions, the CT are considered to reconstruct the overall behavior of the CFD results well. However, although good ZNCCs were obtained for the temperature distributions in all conditions (more than 0.96) and for the concentration distributions in condition 1, 2, and 3 (around 0.94), the values became remarkably worse for the concentration distributions in condition 4 and 5. For a more detailed analysis, the probability distributions of x- and y-direction curvatures were calculated. The x- and y-direction curvatures are defined as the absolute values of $\frac{\partial^2}{\partial x^2} C(x,y)$ and $\frac{\partial^2}{\partial y^2} C(x,y)$ at each grid, respectively. The probability distributions of the curvature for the concentrations of the CFD and the CT in condition 3 that showed the best ZNCC and condition 5 that showed the worst were plotted in Fig. 8. Here, the probability means the ratio of grid number belonging to each class of curvature to the total grid number. The CFD has almost no probability of more than $0.01\% \cdot mm^{-2}$ in condition 3, but it has some probabilities of the curvature in condition 5. The origin of the large curvatures in condition 5 is the local concentration peak around the port 0. On the other hand, the CT has no probability of the curvature in both conditions. Namely, the limitation that the CT cannot reconstruct the local peaks having large curvature of more than $0.01\% \cdot mm^{-2}$ caused the bad ZNCCs in condition 4 and 5. The reason why the CT cannot reconstruct such local peaks is that the minimum spatial resolution is 20 mm in the configuration having 32 laser paths in the circle of 100 mm-diameter [34]. The spatial resolution can be improved if the path number increases. However, as the CT can reconstruct the overall behaviors of distribution when the flow rates were varied, the control of the distributions in the semiconductor chamber by measuring them with the CT-TDLAS is expected to be useful within the limitation.

Table 1 Settings of CH_4 flow rate (slm).

Condition	Port 0	Port 1	Port 2	Port 3
1	0.20	0.20	0.20	0.20
2	0.20	0.10	0.20	0.20
3	0.20	0.10	0.10	0.10
4	0.20	0.40	0.20	0.20
5	0.20	0.40	0.40	0.40

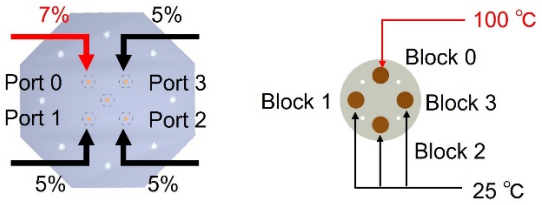

Fig. 5 Settings of CH_4 concentration (left) and heater block temperature (right).

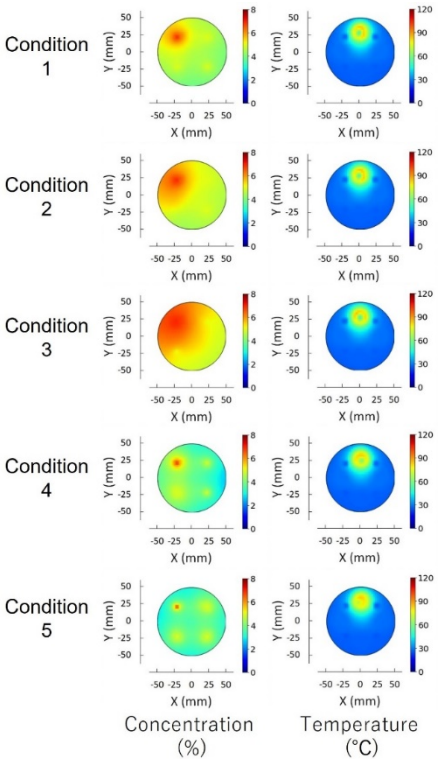

Fig. 6 CFD simulated distributions.

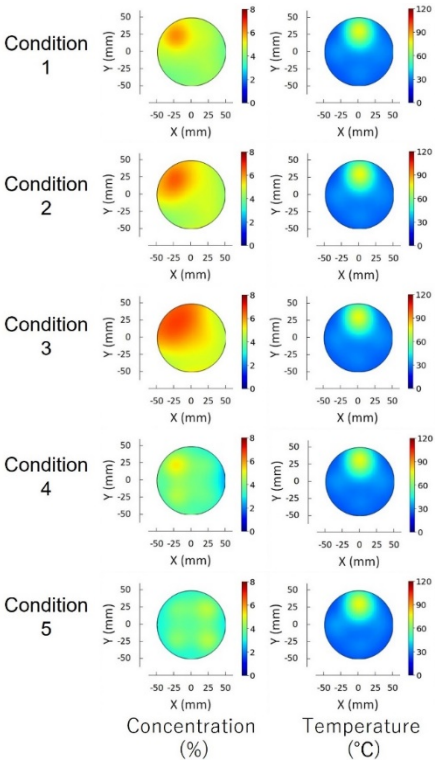

Fig. 7 CT reconstructed distributions.

Table 2 SSD and ZNCC of the reconstructed distributions.

Condition	SSD		ZNCC	
	Concentration	Temperature	Concentration	Temperature
1	0.029	0.043	0.936	0.969
2	0.029	0.047	0.945	0.963
3	0.032	0.047	0.948	0.962
4	0.036	0.045	0.917	0.967
5	0.039	0.045	0.835	0.966

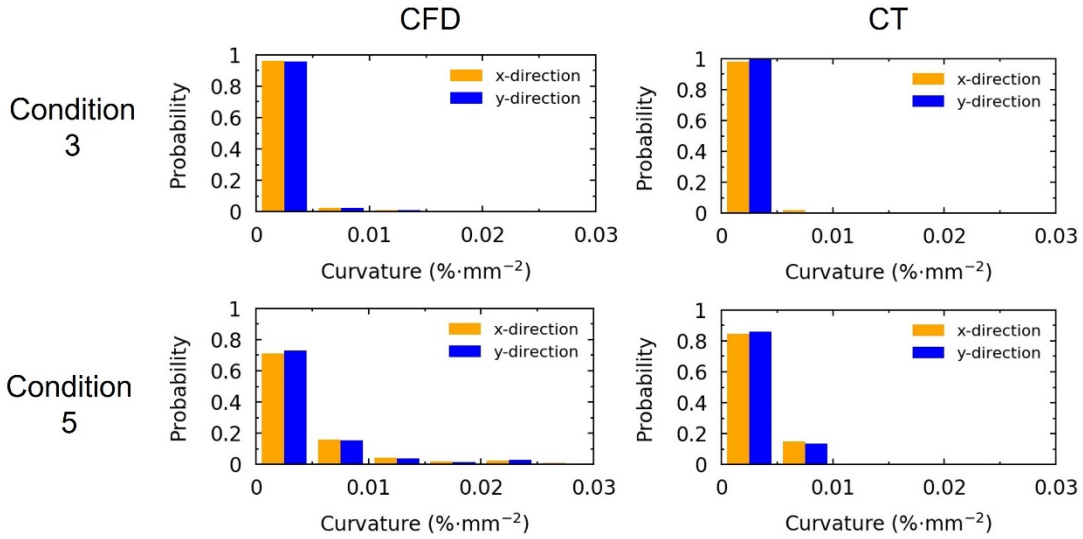

Fig. 8 Probability distributions of the concentration curvatures. The probability is the ratio of grid number belonging to each curvature class to the total grid number.

5. Experimental results and discussions

CH_4 concentration and temperature distributions in the chamber were measured with the CT-TDLAS under the conditions listed in Fig. 5 and Table 1. The measured results are shown in Fig. 9. High concentrations around the port 0 and high temperatures around the block 0 were observed. The results also showed the behaviors that the high concentration area became larger in the order of 1→2→3 and became smaller in the order of 1→4→5 as seen in the CFD. They indicate that the concentration distribution can be controlled by measuring it with the CT-TDLAS and adjusting the flow rates. Due to the spatial resolution limit, controlling local concentration peaks having large curvature of more than $0.01\% \cdot mm^{-2}$ is impossible. However, control to improve concentration uniformity over wafers is considered to be available. Although the relationship between the flow rates and measured concentration distributions showed similar behavior to that of the CFD, the overall levels of measured concentrations in all conditions were higher than the CFD. The reason is that the vacuum powers of the exhaust ports were weaker than considered in the CFD due to the flow impedance originated from the downstream pipe structure [34]. Whereas, the measured temperature distributions were almost the same regardless of the variations of the concentration distribution as seen in the CFD. Therefore, CH_4 temperature distribution over the susceptor can be controlled by adjusting the heater block temperatures in the susceptor, independent of the concentration distribution.

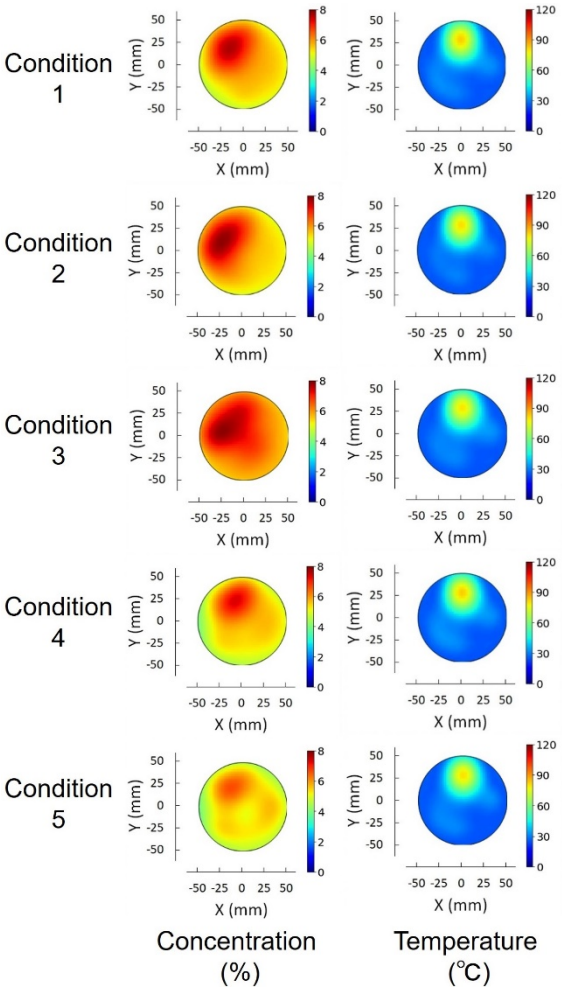

Fig. 9 Measured distributions with CT-TDLAS.

6. Conclusions

In this work, we investigated the feasibility to control the gas concentration and temperature distributions in the semiconductor chamber with the CT-TDLAS. First, the distributions for various CH_4 flow rates under fixing the concentrations injected from the inlet ports and the susceptor temperature were simulated with the CFD. The results indicated the possibility that the concentration distribution is varied by changing the flow rates. They also suggested that the temperature distribution is not influenced by the variations of the concentration distribution. Next, the distributions were reconstructed with CT based on the spectra calculated from the simulated distributions. The CT well reconstructed the overall behavior of the simulated distributions. However, the reproducibility became worse for the distribution having large concentration curvature of more than $0.01\% \cdot mm^{-2}$. Finally, CH_4 was streamed into the chamber under fixed conditions of the concentration injected from inlet ports and susceptor temperature, and the concentration and temperature distributions were measured with the CT-TDLAS. The concentration distributions were varied by changing the flow rates. Therefore, the concentration distribution can be controlled by measuring it with the CT-TDLAS and adjusting the flow rates. However, the controlling the distribution having large concentration curvature of more than $0.01\% \cdot mm^{-2}$ is impossible. As the measured temperature distributions were not influenced by the variations of the concentration distribution, it can be controlled just by adjusting the heater block temperatures in the susceptor.

Throughout this work, the feasibility to control the concentration and temperature distributions in the chamber can be confirmed. The CT-TDLAS measurement and control contribute to improve semiconductor wafer process quality.

References

[1] Ishikawa, K., Ishijima, T., Shiraguji, T., Armini, S., Despiau-Pujo. E., Gattscho, R. A., Kanarik, K. J., Leusink, G. J., Marchack. N., Murayama, T., Morikawa, Y., Oehrin, G. S., Park, S., Hayashi, H., and Kinoshita, K. (2019), Rethinking surface reactions in nanoscale dry process toward atomic precision and beyond: a physics and chemistry perspective, *Jpn. J. Appl. Phys.,* **58,** SE0801.

[2] Kanarik, K. J., Lill, T., Hudson, E. A., Sriraman, S., Tan, S., Marks, J., Vahedi, V., and Gottscho, R. A. (2015), Overview of atomic layer etching in the semiconductor industry, *J. Vac. Sci. Technol. A*, **33,** 020802.

[3] Carver, C. T., Plombon, J. J., Romero, P. E., Suri, S., Tronic, T. A., and Turkot, R. B. Jr. (2015), Atomic Layer Etching: An Industry Perspective, *J. Solid State Sci. Technol.,* **4,** N5005.

[4] Tan, S., Yang, W., Kanarik, K. J., Lill, T., Vahedi, V., Marks, J., and Gottscho, R. A. (2015), Highly selective directional atomic layer etching of sillicon, *J. Solid State Sci. Technol.,* **4,** N5010.

[5] Oehrlein, G. S., Metzler, D., and Li, C. (2015), Atomic layer etching at the tipping point: an overview, *J. Solid State Sci. Technol.,* **4,** N5041.

[6] Kim, T. W., and Aydil, E. S. (2003), Effects of chamber wall conditions on Cl concentration and Si etch rate uniformity in plasma etching reactors, *J. Electrochem. Soc.,* **150,** G418.

[7] Fukasawa, M., Kawashima, A., Kuboi, N, Takagi, H., Tanaka, Y., Sakayori, H., Oshima, K., Nagahata, K., and Tatsumi, T. (2008), Prediction of fluctuations in plasma wall interactions using an EES, *Proc. Dry Process Int. Symp.,* p. 247.

[8] Haq, A. U., Djurdjanovic, D. (2016), Virtual metrology concept for predicting defect levels in semiconductor manufacturing, *Procedia CIRP,* **57,** 580.

[9] Nomura, K., Okazaki, T., Yasuda, S., Kawashima, A., Tani, H., and Matsuda, K. (2011), Virtual metrology of dry etching process characteristics using EES and OES, *Proc. AEC/APC Symp. Asia,* PC-O-018.

[10] Ito, M., Hamaoka, H., Veerasingam, R., Nam, S. K., Sevillano, E., and Nojiri, K. (2012), TEOS etch rate predictions using virtual metrology, *Proc. Int. Symp. Dry Process,* p. 33.

[11] Yasuda, S., Okazaki, T., and Nomura, K. (2013), The VM·APC activities in Sony Semiconductor, *Proc. AEC/APC Symp. Asia,* PC-O-22.

[12] Ropcke, J., Welzel S., Lang, N., Hempel, F., Gatilova, L., Guaitella, O., Rousseau, A., and Davies, P.B. (2008), Diagnostic studies of molecular plasmas using mid-infrared semiconductor lasers, *Appl. Phys. B.,* **92,** 335.

[13] Ropcke, J., Davies, P. B., Hamann, S., Hannemann, M., Lang, N. and van Hleden, H. (2016), Applying Quantum Cascade Laser Spectroscopy in Plasma Diagnostics, *photonics*, **3,** 45.

[14] Lang, N., Zimmermann, S., Zimmermann, H., Macherius, U., Uhlig, B., Schaller, M., Schults, S. E., and Ropke, J. (2015), On treatment of ultra-low-k SiCOH in CF_4 plasmas: correlation between the concentration of etching products and etching rate, *Appl. Phys. B*, **119,** 219.

[15] Hubner, M., Lang, N. Zimmermann, S., Schlz, S. E., Buchholtz, W., Ropcke, J., and van Helden, J. H. (2015), Quantum cascade laser based monitoring of CF_2 radical concentration as a diagnostic tool of dielectric etching plasma processes, *Appl. Phys. Lett.* **106,** 031102.

[16] Hori, M., Kondo, H., and Hiramatsu, M. (2011), Radical-controlled plasma processing for nanofabrication, *Appl. Phys. D*, **44,** 174027.

[17] Lee, C. G. N., Kanarik, K. J., and Gottscho, R. A. (2014), The grand challenges of plasma etching: a manufacturing perspective, *J. Phys. D,* **47,** 273001.

[18] Ishikawa, K., Karahashi, K., Ishijima, T., Cho, S. I., Elliott, S., Hausmann, D., Mocuta, D., Wilson, A., and Kinoshita, K., (2018), Progress in nanoscale dry processes for fabrication of high-aspect-ratio features: How can we control critical dimension uniformity at the bottom? *Jpn. J. Appl. Phys.,* **57,** 06JA01.

[19] Cai, W., and Kaminski, C. F. (2017), Tomographic absorption spectroscopy for the study of gas dynamics and reactive flows, *Prog. Ene. Comb. Sci.,* **59,** 1.

[20] Wright, P., Garcia-Stewart, C. A., Carey, S. J., Hindle, F. P., Pegrum, S. H., Colbourne, S. M., Turner, P. J., Hurr, W. J., Litt, T. J., Murray, S. C., Crossley, S. D., Ozanyan, K. B., and McCann, H. (2005), Toward in-cylinder absorption tomography in a production engine, *App. Opt.,* **44,** 6578.

[21] Wright, P., Terzija, N., Davidson, J. L., Garria-Castillo, S., Garcia-Stewart, C., Pegrum, S., Colbourne, S., Turner, P., Crossley, S. D. Litt, T. Murray, S., Ozanyan, K. B., and MacCann, H. (2010), High-speed chemical species tomography in a multi-cylinder automotive engine, *Chem. Eng. J.,* **158,** 2.

[22] An, X., Kraetschmer, T., Takami, K., Sanders, S. T., Ma, L., Cai, W., Li, X., Roy, S., and Gord, J. R. (2011), Validation of temperature imaging by H_2O absorption spectroscopy using hyperspectral tomography in controlled experiments, *App. Opt.,* **50,** A29.

[23] Liu, C., Xu, L., Cao, Z., and McCann, H., (2014), Reconstruction of axisymmetric temperature and gas concentration distributions by combining fan-beam TDLAS with onion-peeling deconvolution, *IEEE Trans. Instr. Meas.*, **63,** 3067.

[24] Cai, W. and Kaminski, C. F. (2014), A tomographic technique for the simultaneous imaging of temperature, chemical species, and pressure in reactive flows using absorption spectroscopy with frequency-agile laser, *App. Phys. Lett.*, **104,** 034101.

[25] Cai, W. and Kaminski, C. F. (2014), Multiplexed absorption tomography with calibration-free wavelength modulation spectroscopy, *App. Phys. Lett.,* **104,** 154106.
[26] Cai, W. and Kaminski, C. F. (2015), A numerical investigation of high-resolution multispectral absorption tomography for flow thermometry, *App. Phys. B,* **119,** 29.
[27] Sun, P., Zhang, Z., Li, Z., Guo, Q., and Dong, F. (2017), A study of two dimensional tomography reconstruction of temperature and gas concentration in a combustion field using TDLAS, *Appl. Sci.*, **7,** 990.
[28] Kamimoto, T., Deguchi, Y., Choi, D. W., and Shim, J. H. (2016), Validation of the real-time 2D temperature measurement method using the CT tunable diode laser absorption spectroscopy, *Heat Trans. Res.,* **47,** 193.
[29] Deguchi, Y., Kamimoto, T., Wang, Z. Z., Yan, J. J., Liu, J. P., Watanabe, H., and Kurose, R. (2014), Applications of laser diagnostics to thermal power plants and engines, *Appl. Therm. Eng.,* **73,** 1453.
[30] Deguchi, Y., Kamimoto, T., and Kiyota, Y. (2015), Time resolved 2D concentration and temperature measurement using tunable laser absorption spectroscopy, *Flow Meas. Instr.,* **46,** 312.
[31] Kamimoto, T. and Deguchi, Y. (2015), Temperature detection characteristics of engine exhaust gases using tunable diode laser absorption spectroscopy, *Int. J. Mech. Syst. Eng.,* **1,** 109.
[32] Matsui, H., Udagawa, K., Deguchi, Y., and Kamimoto, T. (2019), Simultaneous two cross-sectional measurements of NH_3 concentration in bent pipe flow using CT-tunable diode laser absorption spectroscopy, *J. Therm. Sci. Tech.,* **14,** JTST0016.
[33] Ma, L., Li, X., Sanders, S. T., Caswell, A. W., Roy, S., Plemmons, D. H., and Gord, J. R. (2013), 50-kHz-rate 2D imaging of temperature and H_2O concentration at the exhaust plane of a J85 engine using hyperspectral tomography, *Opt. Exp.,* **21,** 1152.
[34] Hayashi, D., Nakai, J., Minami, M., Fujita, K., Kamimoto, T., and Deguchi, Y. (2018) CH_4 concentration distribution in a semiconductor process chamber measured by the CT-TDLAS, *J. Solid State Sci. Technol.,* **7,** Q211.
[35] Hayashi, D., Nakai, J., Minami, M., Kamimoto, T., and Deguchi, Y. (2019), Simultaneous measurement of CH4 concentration and temperature distributions in a semiconductor process chamber, *J. Phys. D.*, **52,** 485107.
[36] Lackner, M. (2007), Tunable diode laser absorption spectroscopy (TDLAS) in the process industries – a review, *Rev. Chem. Eng.,* **23,** 65.
[37] Allen, M. G. (1998), Diode laser absorption sensors for gas-dynamic and combustion flows, *Meas. Sci. Technol.,* **9,** 545.
[38] Ma, L. and Cai, W. (2008), Numerical investigation of hyperspectral tomography for simultaneous temperature and concentration imaging, *App. Opt.,* **47,** 3751.
[39] Kasyutich, V. L., Martin, P. A. (2011), Towards a two-dimensional concentration and temperature laser absorption tomography sensor system, *Appl. Phys. B*, **102,** 149.
[40] Wang, F., Cen, K. F., Li, N., Jefferies, J. B., Huang, Q. X., Yan, J. H., and Chi, Y. (2010), Two-dimensional tomography for gas concentration and temperature distributions based on tunable diode laser absorption spectroscopy, *Meas. Sci. Technol.,* **21,** 045301.
[41] Liu, C., Xu, L., Chen, J., Cao, Z., Lin, Y., and Cai, W. (2015), Development of a fan-beam TDLAS-based tomographic sensor for rapid imaging of temperature and gas concentration, *Opt. Exp.,* **23,** 22494.

ISSN 2475-4811, eISSN 2475-482X /$- see front materials
DOI:10.5890/JVTSD.2017.03.001